Configuration and Operation of Nine-Arm Modular Multilevel Converter With Improved Hybrid Submodules

Futian Qin, *Student Member, IEEE*, Feng Gao, *Senior Member, IEEE*, Yi Tang, *Senior Member, IEEE*, Tao Xu, *Member, IEEE*, Jinyu Wang, *Member, IEEE*, and Decun Niu, *Student Member, IEEE*

***Abstract*—This article proposes a new nine-arm modular multilevel converter (9A-MMC) with improved hybrid submodules for middle arms. In specific, the middle arms are formed by the unidirectional current full-bridge submodules (UC-FBSMs), while the upper and lower arms are formed by the traditional half-bridge submodules (HBSMs). Compared with the standard 9A-MMC where the upper, middle, and lower arms are all formed by HBSMs, the dc-side voltage of the new 9A-MMC can be reduced by one-third, and whose switch count is the same as that of the standard 9A-MMC. Moreover, the dc offset in the common mode voltages (CMVs) of the new 9A-MMC is eliminated. In this article, the middle arm current of the new 9A-MMC was thoroughly discussed, and the maximum operation range of the new 9A-MMC was also presented. To enlarge the operation range of the proposed 9A-MMC, a middle arm current reshaping control method was put forward as well. The feasibility and performance characteristics of the proposed 9A-MMC were finally verified by the simulation and experimental results.**

***Index Terms*—Modular multilevel converter (MMC), nine-arm modular multilevel converter (9A-MMC), submodule (SM), arm current control.**

I. Introduction

SINCE modular multilevel converter (MMC) was first proposed in [1], [2], it has drawn the increasing interests and become one of the most promising multilevel topologies in medium/high-voltage applications, such as high-voltage direct current (HVdc) transmission systems [3]–[5], flexible ac transmission systems (FACTs) [6]–[8], medium-voltage motor drives [9], [10], etc., due to its prominent advantages of modularity, scalability, and superior harmonic performances [11]–[13].

There are several medium/high-voltage applications including two sets of three-phase terminals, such as medium-voltage dual-motor drives, unified power flow controller (UPFC), where two independent MMCs were generally employed [8], [14]. Fortunately, it is possible to integrate two MMCs into one compact nine-arm MMC (9A-MMC) with two sets of three-phase terminals [15]–[18]. Compared with two independent MMCs, 9A-MMC can save 25% of the required arms and 50% of the arm inductors to reduce system volume, weight, and cost.

The 9A-MMC was first proposed in [19], where the dc-side of submodules (SMs) in the 9A-MMC was replaced by ideal dc sources to simplify the control scheme design, the circulating current suppression control (CCSC) and capacitor voltage balancing control (CVBC) were not considered in [19]. The detailed operation analysis and control scheme of 9A-MMC including CCSC and CVBC were presented in [20], [21]. Moreover, the operation range of 9A-MMC is limited, and the dc-side voltage is increased by 50% compared with the conventional MMC. Therefore, a unique operation mode of 9A-MMC that the number of SMs in each arm can be different was presented in [21], and the operation range limitation of 9A-MMC can be eliminated by the elaborate design of the number of SMs in each arm. However, under this unique operation mode, the number of SMs will be increased when the amplitude of two output voltages and the relative phase angle between two output terminals are large, which means the advantages of reduced system cost and size in 9A-MMC will be not obvious. Besides, the dc-side voltage of 9A-MMC needs to be varied with the sum of SM number in one phase under this unique operation mode.

In the implementation, the common mode voltage (CMV) generated by the 9A-MMC has a large dc offset, which is caused by the unique topological features in nature and can limit its application. For example, in the 220kV western Nanjing UPFC project which has been put into commercial operation in December 2015, both the shunt-side and series-side transformers are designed to be grounded, if the 9A-MMC is assumed, the dc current will be introduced into the transformer and then saturate the transformer core and increase the transformer vibration, noise, and reactive power losses [22].

It is noted that the 9A-MMC presented in [15]–[21] was only formed by half-bridge submodules (HBSMs), which can be

Manuscript received May 1, 2020; revised September 10, 2020; accepted October 22, 2020. Date of publication October 30, 2020; date of current version February 5, 2021. This work was supported in part by the National Natural Science Foundation of China under Grant 51722704, in part by the Foundation for Innovative Research Groups of National Natural Science Foundation of China under Grant 61821004, and in part by the Key Project of National Natural Science Foundation of China under Grant 61733010. *(Corresponding author: Feng Gao.)*

Futian Qin, Tao Xu, Jinyu Wang, and Decun Niu are with the Key Laboratory of Power System Intelligent Dispatch and Control of Ministry of Education, Jinan 250061, China (e-mail: ft_qin@163.com; xutaojason@163.com; jinyu88330@126.com; niudecun@126.com).

Feng Gao is with the School of Control Science and Engineering, Shandong University, Jinan 250061 Singapore, China (e-mail: fgao@sdu.edu.cn).

Yi Tang is with the School of Electrical and Electronic Engineering, Nanyang Technological University, Singapore 639798, Singapore (e-mail: yitang@ntu.edu.sg).

Color versions of one or more of the figures in this article are available online at https://ieeexplore.ieee.org.

Digital Object Identifier 10.1109/TPEL.2020.3034921

named as standard 9A-MMC in the following for distinguishing from the hybrid 9A-MMC. In [23], a hybrid 9A-MMC was proposed to feed a medium-voltage six-phase induction machine, where the middle arms are not composed of the HBSMs but the conventional full-bridge submodules (FBSMs). With the benefit of the negative-voltage level generated by the FBSM, the hybrid 9A-MMC can eliminate the operation range limitation of the standard 9A-MMC, and the dc-side voltage of the hybrid 9A-MMC can be reduced as well. But, the semiconductor count of the hybrid 9A-MMC is increased by one-third compared with the standard 9A-MMC.

However, this article proposes a new 9A-MMC, where the middle arms are formed by the unidirectional current FBSMs (UC-FBSMs), while the upper and lower arms are still formed by the HBSMs. Compared with the standard 9A-MMC, the dc-side voltage of the new 9A-MMC can be reduced by one-third being the same as the conventional MMC, and the switch count of the new 9A-MMC is the same as that of the standard 9A-MMC. Moreover, there is no longer a dc offset in the CMVs of the new 9A-MMC. To enlarge the operation range of the proposed 9A-MMC, this article proposes a middle arm current reshaping control method. Finally, the simulation and experimental results verified the performance of the proposed new 9A-MMC.

II. Topology and Mathematical Model of the Proposed 9A-MMC

A. Topology

Fig. 1 illustrates the new 9A-MMC, which consists of three phase-legs, and each phase-leg has three arms, the upper, middle, and lower arms. The upper and lower arms are composed of N series-connected identical HBSMs, while the middle arms are composed of N series-connected identical UC-FBSMs. L_u and L_l are the arm inductors in the upper and lower arms, respectively. Generally, $L_u = L_l$. There are two sets of three-phase ac terminals: one locates at the middle point between upper and middle arms, and the other locates at the middle point between the middle and lower arms.

The UC-FBSM can be regarded as a simplified FBSM as shown in Fig. 2(a), where two switches (S_1, S_4) are replaced by two diodes (D_1, D_4). The current paths of the UC-FBSM when the current is positive (flowing into the submodule) and negative (flowing out of the submodule) under the different switch states are presented in Fig. 2(b) and (c), respectively. It is worth noting that the current path of the UC-FBSM when the current is negative is not related to the states of the switches (S_2, S_3), which means the UC-FBSM is uncontrollable when the current is negative. Moreover, the capacitor in UC-FBSM will be always charged when the current is negative. Therefore, the operation state of the UC-FBSM when the current is negative should only appear in the process of the SM pre-charging [24]. Under normal operation, the current of the UC-FBSM should be always positive. As shown in Fig. 2(b), D_2 and D_3 in the UC-FBSM will be unnecessary when the current is always positive, and the current rating of D_2 and D_3 can be lower than that of the other semiconductors. Although the current of the UC-FBSM is unidirectional under the normal operation, the capability of

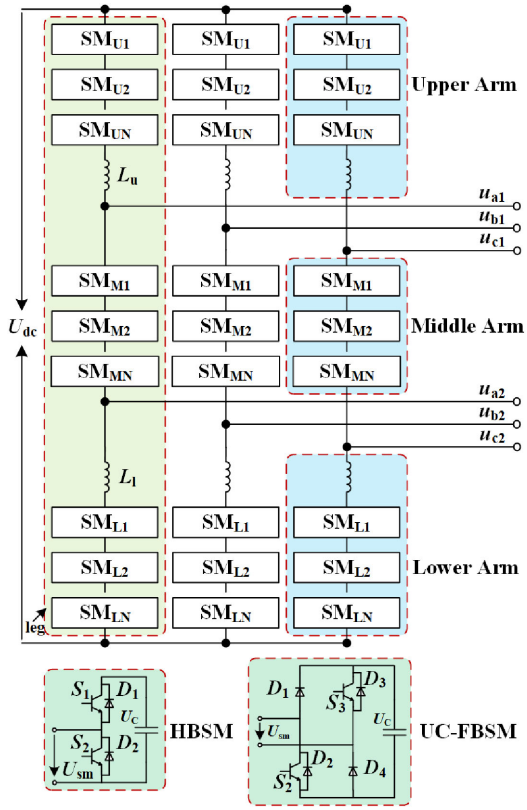

Fig. 1. Topology of the proposed nine-arm modular multilevel converter (9A-MMC).

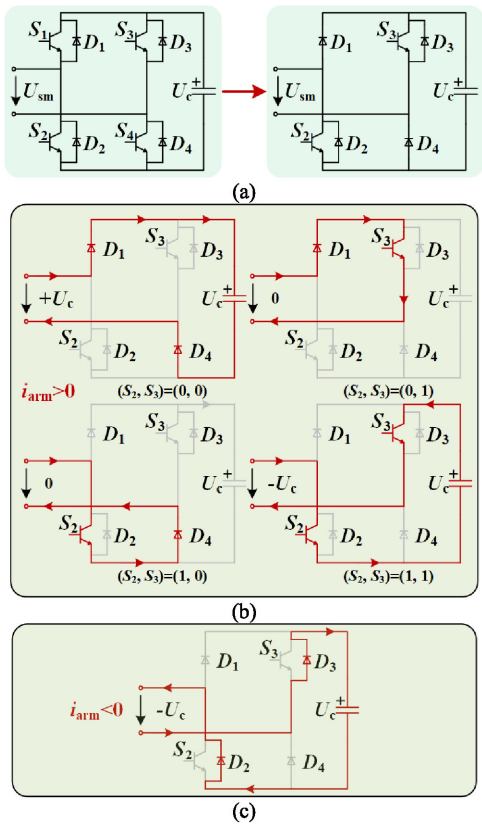

Fig. 2. (a) Unidirectional current full bridge submodule (UC-FBSM), and its current paths when the current is (b) positive or (c) negative.

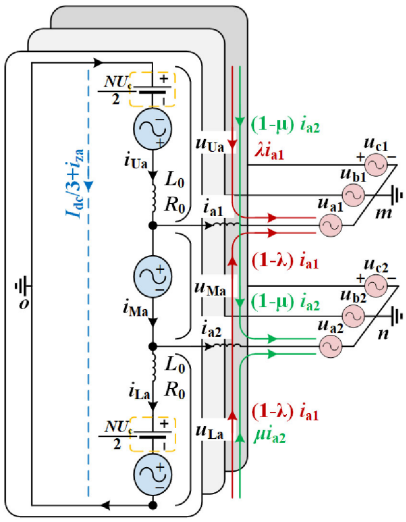

Fig. 3. Equivalent model of the three-phase new 9A-MMC.

generating negative-voltage levels like conventional FBSM is inherited in the UC-FBSM.

B. Mathematical Model

The simplified equivalent model of the proposed three-phase 9A-MMC is presented in Fig. 3, where the SMs are considered as the controlled voltage sources and the voltage of each arm is the combination of these controlled voltage sources. According to Fig. 3, the mathematical expressions of the upper, middle, and lower arms' voltages and currents of phase j ($j = a$, b or c) in the new 9A-MMC can be derived as:

$$u_{\mathrm{Uj}} = (NU_c)/2 - u_{jo1} - \left(L_0 \frac{di_{\mathrm{Uj}}}{dt} + R_0 i_{\mathrm{Uj}}\right) \tag{1}$$

$$u_{\mathrm{Mj}} = u_{jo1} - u_{jo2} \tag{2}$$

$$u_{\mathrm{Lj}} = (NU_c)/2 + u_{jo2} - \left(L_0 \frac{di_{\mathrm{Lj}}}{dt} + R_0 i_{\mathrm{Lj}}\right) \tag{3}$$

$$i_{\mathrm{Uj}} = I_{\mathrm{dc}}/3 + \lambda i_{j1} + (1-\mu) i_{j2} + \sum_{n=2}^{+\infty} i_{zj}^{(\mathrm{n})} \tag{4}$$

$$i_{\mathrm{Mj}} = I_{\mathrm{dc}}/3 - (1-\lambda) i_{j1} + (1-\mu) i_{j2} + \sum_{n=2}^{+\infty} i_{zj}^{(\mathrm{n})} \tag{5}$$

$$i_{\mathrm{Lj}} = I_{\mathrm{dc}}/3 - (1-\lambda) i_{j1} - \mu i_{j2} + \sum_{n=2}^{+\infty} i_{zj}^{(\mathrm{n})} \tag{6}$$

where (u_{Uj}, u_{Mj}, u_{Lj}) and (i_{Uj}, i_{Mj}, i_{Lj}) are, respectively, the upper, middle, and lower arm voltages and currents of phase j; (u_{jo1}, u_{j02}) and (i_{j1}, i_{j2}) are, respectively, the converter upper and lower output voltages and currents of phase j; N is the number of SMs in each arm; U_c is the rated SM capacitor voltage; L_0 and R_0 are, respectively, the inductance and resistance of the arm inductor; λ and μ are, respectively, the distribution coefficients of the upper and lower output currents among three arms; I_{dc} is the dc-side current, and $i_{\mathrm{zj}}^{(n)}$ is the nth-order circulating current of phase j.

Moreover, the converter upper and lower output voltages (u_{jo1}, u_{j02}) can be separately decomposed into two parts, which can be expressed as

$$u_{jo1} = u_{j1} + u_{\mathrm{mo}} \tag{7}$$

$$u_{jo2} = u_{j2} + u_{\mathrm{no}} \tag{8}$$

where u_{j1} and u_{j2} are the upper and lower output phase voltages, respectively, and u_{mo} and u_{no} are the common mode voltages of the upper and lower output terminals, respectively.

Neglecting the arm inductor voltages, and according to (1)–(3), the relationships of the converter output voltages (u_{jo1}, u_{j02}) and the arm voltages (u_{Uj}, u_{Mj}, u_{Lj}) can be derived as

$$u_{jo1} = (u_{\mathrm{Mj}} + u_{\mathrm{Lj}} - u_{\mathrm{Uj}})/2 \tag{9}$$

$$u_{jo2} = (u_{\mathrm{Lj}} - u_{\mathrm{Mj}} - u_{\mathrm{Uj}})/2. \tag{10}$$

Finally, the CMVs of the upper and lower output terminals in the proposed 9A-MMC can be obtained as

$$\begin{aligned} u_{\mathrm{mo}} &= u_{jo1} - u_{j1} = (u_{\mathrm{Mj}} + u_{\mathrm{Lj}} - u_{\mathrm{Uj}})/2 - u_{j1} \\ &= (u_{\mathrm{Ma}} + u_{\mathrm{La}} - u_{\mathrm{Ua}} + u_{\mathrm{Mb}} + u_{\mathrm{Lb}} - u_{\mathrm{Ub}} + u_{\mathrm{Mc}} + u_{\mathrm{Lc}} \\ &\quad - u_{\mathrm{Uc}})/6 \end{aligned} \tag{11}$$

$$\begin{aligned} u_{\mathrm{no}} &= u_{jo2} - u_{j2} = (u_{\mathrm{Lj}} - u_{\mathrm{Mj}} - u_{\mathrm{Uj}})/2 - u_{j2} \\ &= (u_{\mathrm{La}} - u_{\mathrm{Ma}} - u_{\mathrm{Ua}} + u_{\mathrm{Lb}} - u_{\mathrm{Mb}} - u_{\mathrm{Ub}} + u_{\mathrm{Lc}} - u_{\mathrm{Mc}} \\ &\quad - u_{\mathrm{Uc}})/6. \end{aligned} \tag{12}$$

In comparison, according to the operation analysis of the standard 9A-MMC in [21], the CMVs (u'_{mo}, u'_{no}) of the standard 9A-MMC can be expressed as

$$\begin{aligned} u'_{\mathrm{mo}} &= (u'_{\mathrm{Mj}} + u'_{\mathrm{Lj}} - u'_{\mathrm{Uj}})/2 - u'_{j1} \\ &= (u'_{\mathrm{Ma}} + u'_{\mathrm{La}} - u'_{\mathrm{Ua}} + u'_{\mathrm{Mb}} + u'_{\mathrm{Lb}} - u'_{\mathrm{Ub}} + u'_{\mathrm{Mc}} \\ &\quad + u'_{\mathrm{Lc}} - u'_{\mathrm{Uc}})/6 - (NU_c)/4 \end{aligned} \tag{13}$$

$$\begin{aligned} u'_{\mathrm{no}} &= (u'_{\mathrm{Lj}} - u'_{\mathrm{Mj}} - u'_{\mathrm{Uj}})/2 - u'_{j2} \\ &= (u'_{\mathrm{La}} - u'_{\mathrm{Ma}} - u'_{\mathrm{Ua}} + u'_{\mathrm{Lb}} - u'_{\mathrm{Mb}} - u'_{\mathrm{Ub}} + u'_{\mathrm{Lc}} \\ &\quad - u'_{\mathrm{Mc}} - u'_{\mathrm{Uc}})/6 + (NU_c)/4. \end{aligned} \tag{14}$$

As shown in (11) and (12), there is no dc offset in the CMVs of the proposed 9A-MMC being similar to that of the conventional MMC, which is mainly dominated by the PWM modulation scheme [25].

In addition, the dc-side voltage U_{dc} of the proposed 9A-MMC can be derived as

$$U_{\mathrm{dc}} = (u_{\mathrm{Uj}} + u_{\mathrm{Mj}} + u_{\mathrm{Lj}}) = NU_c. \tag{15}$$

The dc-side voltage of the standard 9A-MMC U'_{dc} is

$$U'_{\mathrm{dc}} = (u'_{\mathrm{Uj}} + u'_{\mathrm{Mj}} + u'_{\mathrm{Lj}}) = (3NU_c)/2. \tag{16}$$

Compared with the standard 9A-MMC, the dc-side voltage of the proposed 9A-MMC can be reduced by one-third, which is the same as that of the conventional MMC. Therefore, the insulation issue of the new 9A-MMC can be treated the same as the conventional MMC.

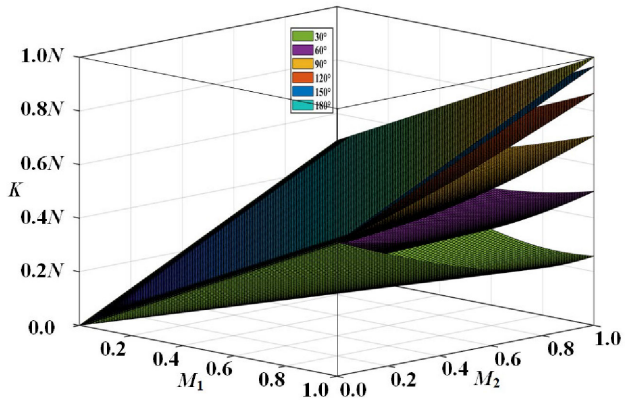

Fig. 4. Value of K with the variation of M_1 and M_2 under different θ.

III. Operation Analysis of the Proposed 9A-MMC

A. Required SM Count in Middle Arm of the Proposed 9A-MMC

Although the number of SMs in the middle arm of the proposed 9A-MMC is designed to be the same as that in the upper and lower arms, the number of SMs in the middle arm actually can be fewer than N in the actual operation. Because, as long as the total SM capacitor voltages in the middle arm are always greater than the absolute middle arm reference voltage, the normal operation of the proposed 9A-MMC can be guaranteed.

The upper and lower output phase voltages can be assumed to be

$$u_{j1}(t) = U_{j1}\sin(\omega t) \tag{17}$$

$$u_{j2}(t) = U_{j2}\sin(\omega t + \theta) \tag{18}$$

where U_{j1} and U_{j2} are the amplitudes of the upper and lower output phase voltages, respectively, and θ is the relative phase angle between two output terminals. Substituting (17) and (18) into (1)–(3), and neglecting the arm inductor voltages, the normalized reference voltages of the upper, middle, and lower arms in the proposed 9A-MMC can be calculated as:

$$u_{\mathrm{Uj}}(t) = \left[1 - M_1\sin(\omega t)\right]/2 \tag{19}$$

$$u_{\mathrm{Mj}}(t) = \left[M_1\sin(\omega t) - M_2\sin(\omega t + \theta)\right]/2 \tag{20}$$

$$u_{\mathrm{Lj}}(t) = \left[1 + M_2\sin(\omega t + \theta)\right]/2 \tag{21}$$

where $M_1 = (2U_{j1})/(NU_c)$ and $M_2 = (2U_{j2})/(NU_c)$ denote the modulation ratios of the upper and lower output terminals, respectively.

Therefore, the number of required SMs in the middle arm can be expressed as:

$$K = \mathrm{ceil}\left[\mathrm{N}\sqrt{\left\{\frac{\mathrm{M}_1}{2} - \frac{\mathrm{M}_2}{2}\cos(\theta)\right\}^2 + \left\{\frac{\mathrm{M}_2}{2}\sin(\theta)\right\}^2}\right] \tag{22}$$

where ceil is the top integral function.

To clearly illustrate the range of K, the 3-D curves of the maximum M_1, M_2, and K under different θ are presented in Fig. 4. It can be seen that the maximum value of K is equal to N when $M_1 = M_2 = 1$ and θ is set as 180°. In other operation conditions, the value of K is fewer than N. Therefore, the (N-K) SMs in the middle arms of the proposed 9A-MMC can be bypassed to reduce the power losses during operation.

B. Analysis of Middle Arm Current in the Proposed 9A-MMC

Due to the unique topology of UC-FBSM, the middle arm current should be always positive under the normal operation as addressed in Section II-A. According to (5), the middle arm current is significantly related to the distribution coefficients (λ, μ). To obtain the middle arm current at certain operation states, the distribution coefficients (λ, μ) should be first determined.

The upper and lower output currents of the proposed 9A-MMC can be assumed to be

$$i_{j1}(t) = I_{j1}\sin(\omega t - \varphi_1) \tag{23}$$

$$i_{j2}(t) = I_{j2}\sin(\omega t + \theta - \varphi_2) \tag{24}$$

where I_{j1} and I_{j2} are the amplitudes of upper and lower output currents, respectively, and φ_1 and φ_2 are the power factor angles of the upper and lower output terminals, respectively.

Substituting (23) and (24) into (4)–(6), and assuming the circulating currents to be suppressed effectively, three arm currents can be expressed as

$$\begin{aligned} i_{\mathrm{Uj}}(t) &= I_{\mathrm{dc}}/3 + \lambda I_{j1}\sin(\omega t - \varphi_1) \\ &\quad + (1-\mu)I_{j2}\sin(\omega t + \theta - \varphi_2) \end{aligned} \tag{25}$$

$$\begin{aligned} i_{\mathrm{Mj}}(t) &= I_{\mathrm{dc}}/3 - (1-\lambda)I_{j1}\sin(\omega t - \varphi_1) \\ &\quad + (1-\mu)I_{j2}\sin(\omega t + \theta - \varphi_2) \end{aligned} \tag{26}$$

$$\begin{aligned} i_{\mathrm{Lj}}(t) &= I_{\mathrm{dc}}/3 - (1-\lambda)I_{j1}\sin(\omega t - \varphi_1) \\ &\quad - \mu I_{j2}\sin(\omega t + \theta - \varphi_2). \end{aligned} \tag{27}$$

The average absorbed power of each arm can be calculated by multiplying the corresponding arm voltage with arm current, which can be expressed as

$$\begin{aligned} &p_{\mathrm{Uj}} \\ &= \frac{1}{T}\int_0^T (\frac{1}{2}NU_c - u_{j1}) \times [\frac{1}{3}I_{\mathrm{dc}} + \lambda i_{j1} + (1-\mu)i_{j2}]dt \\ &= \frac{NU_cI_{\mathrm{dc}}}{6} - \frac{\lambda I_{j1}U_{j1}\cos(\varphi_1)}{2} - \frac{(1-\mu)I_{j2}U_{j1}\cos(\theta-\varphi_2)}{2} \end{aligned} \tag{28}$$

$$\begin{aligned} &p_{\mathrm{Mj}} \\ &= \frac{1}{T}\int_0^T (u_{j1} - u_{j2}) \times [\frac{1}{3}I_{\mathrm{dc}} - (1-\lambda)i_{j1} + (1-\mu)i_{j2}]dt \\ &= -\frac{(1-\lambda)I_{j1}U_{j1}\cos(\varphi_1)}{2} - \frac{(1-\mu)I_{j2}U_{j2}\cos(\varphi_2)}{2} \\ &\quad + \frac{(1-\mu)I_{j2}U_{j1}\cos(\theta-\varphi_2)}{2} + \frac{(1-\lambda)I_{j1}U_{j2}\cos(\theta+\varphi_1)}{2} \end{aligned} \tag{29}$$

$$\begin{aligned} &p_{\mathrm{Lj}} \\ &= \frac{1}{T}\int_0^T (\frac{1}{2}NU_c + u_{j2}) \times [\frac{1}{3}I_{\mathrm{dc}} - (1-\lambda)i_{j1} - \mu i_{j2}]dt \\ &= \frac{NU_cI_{\mathrm{dc}}}{6} - \frac{(1-\lambda)I_{j1}U_{j2}\cos(\theta+\varphi_1)}{2} - \frac{\mu I_{j2}U_{j2}\cos(\varphi_2)}{2}. \end{aligned} \tag{30}$$

Moreover, the dc-side current of the proposed 9A-MMC can be written as:

$$I_{\rm dc} = \frac{3[I_{j1}U_{j1}\cos(\varphi_1) + I_{j2}U_{j2}\cos(\varphi_2)]}{2NU_c} \quad (31)$$

The transferred active power between dc-side and ac-side is equal under the steady states. This means that there is no active power absorbed by three arms. Hence, $p_{\rm Uj}$, $p_{\rm Mj}$, and $p_{\rm Lj}$ should be equivalent to 0 when the converter works under a steady state. The distribution coefficients (λ, μ) can be solved by (28)–(30), and the middle arm current at the certain operation conditions can be calculated after obtaining (λ, μ).

To intuitively reveal the middle arm current in the new 9A-MMC, the middle arm current shown in (26) is rewritten as

$$i_{\rm Mj}(t) = I_{\rm dc}/3 + \sqrt{A^2 + B^2}\sin(\omega t + \alpha) \quad (32)$$

where A, B, and α can be expressed as

$$A = -(1-\lambda)I_{j1}\cos(\varphi_1) + (1-\mu)I_{j2}\cos(\theta - \varphi_2) \quad (33)$$

$$B = (1-\lambda)I_{j1}\sin(\varphi_1) + (1-\mu)I_{j2}\sin(\theta - \varphi_2) \quad (34)$$

$$\alpha = \arctan(B/A). \quad (35)$$

As shown in (32), the middle arm current can be divided into three scenarios according to the amplitude of ac component in the middle arm current, and the analysis of each scenario can be conducted as follows:

1) $\sqrt{A^2 + B^2} = 0$*:* If the amplitude of the ac component in middle arm current is equal to 0 (i.e., there is no ac component in the middle arm current), the middle arm current will only consist of the dc component. The upper output current i_{j1} will only follow through the upper arm, the lower output current i_{j2} will only follow through the lower arm. It can be seen that if the amplitude of the ac component in the middle arm current wants to be equal to 0, both λ and μ should be equal to 1. Therefore, when both λ and μ are equal to 1, there is only a dc component in the middle arm current, and no extra middle arm current control is required.

2) $\sqrt{A^2 + B^2} \le I_{\rm dc}/3$*:* According to (32), even if there are ac components in the middle arm current, the middle arm current will still be positive as long as the amplitude of the ac component is equal or smaller than the dc component. The amplitudes of the dc and ac component in middle arm current can be calculated by (31) and (33)–(34), respectively. Then, the operation range that the amplitude of the ac component in the middle arm current is equal or smaller than the dc component can be easily obtained. Fig. 5(a) displays the amplitude change of the ac and dc components in the middle arm current when both M_1 and M_2 vary from 0.0 to 1.0, θ is set as 60°, where the design parameters of the proposed 9A-MMC are listed in Table I. The operation ranges that the middle arm current is positive and bidirectional are shown in Fig. 5(b). Being similar to the first scenario, there is no need to design any extra middle arm current control.

3) $\sqrt{A^2 + B^2} > I_{\rm dc}/3$*:* If the amplitude of the ac component in the middle arm current is larger than the dc component, the middle arm current will be bidirectional, which is not allowed under the normal operation of the proposed 9A-MMC. The operation range that the middle arm current is bidirectional when both M_1 and M_2 vary from 0.0 to 1.0 and θ is set as 60° is also presented in Fig. 5. To enlarge the operation range of the proposed 9A-MMC, the middle arm current should be intentionally regulated to keep positive.

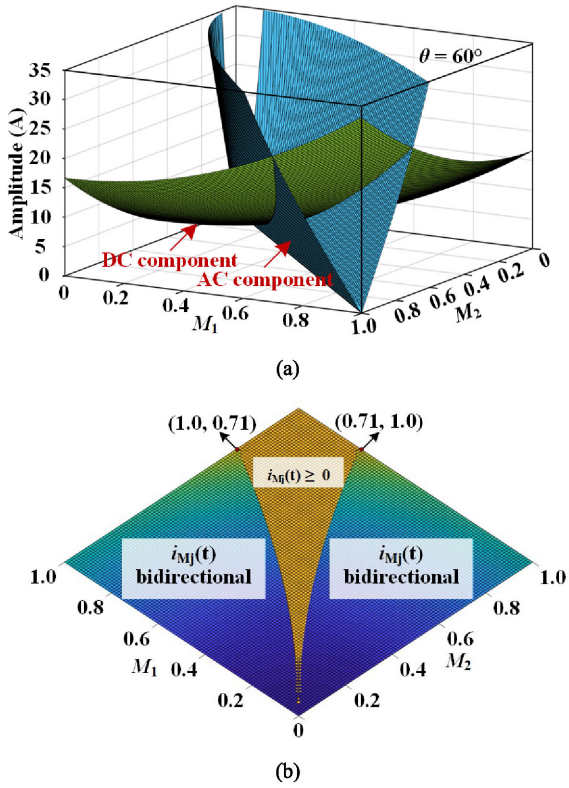

Fig. 5. (a) Amplitude variation of the dc and ac components in the middle arm current, and (b) the operation range that the middle arm is positive or bidirectional.

TABLE I
COMPARISONS BETWEEN STANDARD AND NEW 9A-MMC

	Standard 9A-MMC	New 9A-MMC
DC voltage	$U_{\rm dc}$	$2U_{\rm dc}/3$
Number of SMs	$9N$ HBSMs	$6N$ HBSMs +$3N$ UC-FBSMs
SM capacitor voltage	$U_{\rm dc}/(3N)$	$U_{\rm dc}/(3N)$
Number of SM capacitors	$9N$	$9N$
Number of IGBTs	$18N$	$18N$
Number of Diodes	$18N$	$24N$
DC offset in CMV	Yes	No

According to (33) and (34), the amplitude of the ac component in the middle arm current at certain operation conditions depends on the distribution coefficients λ and μ. Therefore, the amplitude of the ac component can be regulated by adjusting λ and μ. In principle, the middle arm current can be controlled by flexibly regulating the SM capacitor voltages of upper and lower arms. In conventional MMC, the SM capacitor voltages of the upper and lower arms are generally controlled to be identical. But being different, the SM capacitor voltages of the upper and lower arms of the proposed 9A-MMC will be unequal. The maximum operation range of the proposed 9A-MMC with and without middle arm current reshaping are shown in Fig. 6. It can be seen

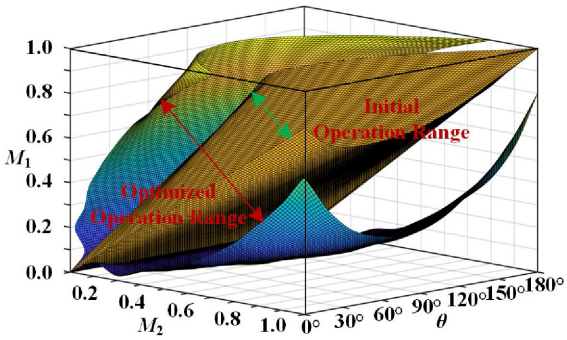

Fig. 6. Initial operation range without the middle arm current reshaping control and the optimized operation range with the middle arm current reshaping control of the proposed 9A-MMC.

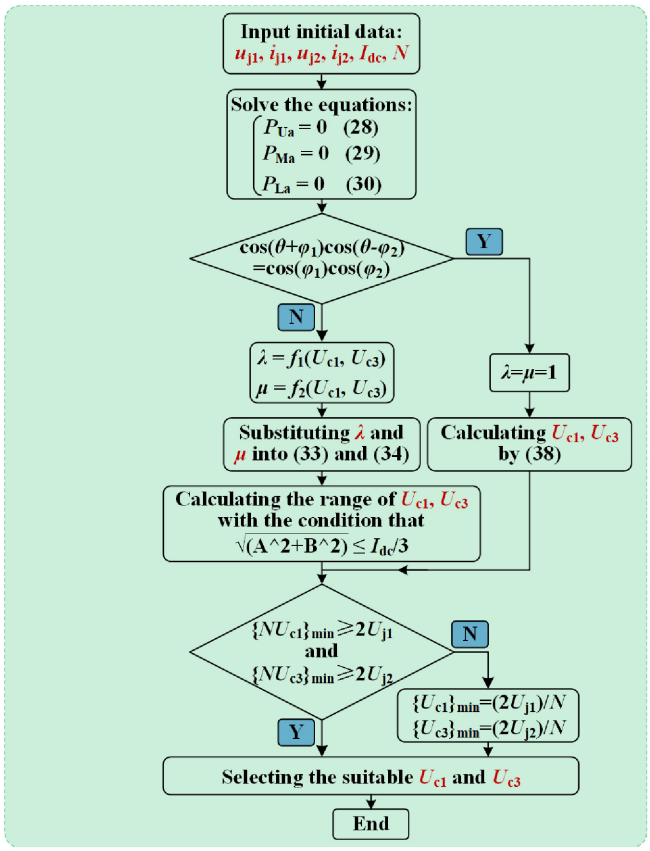

Fig. 7. Middle arm current reshaping control method.

that the operation range of the proposed 9A-MMC is expanded by shaping the middle arm current.

To clearly show the benefits of the new 9A-MMC, the comparisons with the standard 9A-MMC are summarized in Table I.

IV. Control Scheme of the Proposed 9A-MMC

Fig. 7 shows the procedures of the proposed middle arm current reshaping control method. Under certain operation conditions, the equations about λ and μ taking (U_{c1}, U_{c3}) as variables can be obtained by solving the (28)–(30), when $[\cos(\theta+\varphi_1)\cos(\theta-\varphi_2)-\cos(\varphi_1)\cos(\varphi_2)] \neq 0$

Equations (36) and (37), shown at the bottom of the next page, are usually preprocessed by input initial data. Then, the processed (36) and (37) are substituted into (33) and (34), and thus, the equations about A and B taking (U_{c1}, U_{c3}) as variables can be deduced. Finally, the range of (U_{c1}, U_{c3}) can be obtained by solving the inequality $\sqrt{A^2+B^2} \le I_{dc}/3$. The inequality can be finally expressed as $aU_{c1}^2+bU_{c1}+c \le 0$, where ($a$, b, c) are the simple numbers, which are related to the input data. It is noted that the coefficient a is positive due to square operation. The final inequality can be solved by the simple calculation program, and the flowchart of the calculation program is shown in Fig. 8. Moreover, the selection of (U_{c1}, U_{c3}) should consider the following criteria. The first is to avoid the over-modulation, the summed SM capacitor voltages of the upper and lower arms should be larger than the double amplitude of the upper and lower output phase voltage, respectively. The second is that under the premise of the normal operation, the SM capacitor voltage should be as small as possible to reduce the voltage stress of semiconductors.

When $[\cos(\theta+\varphi_1)\cos(\theta-\varphi_2)-\cos(\varphi_1)\cos(\varphi_2)]=0$, λ and μ in (36) and (37) are no longer suitable. Instead, $\lambda=\mu=1$ can be obtained by solving (28)–(30) under the above condition. Besides, (U_{c1}, U_{c3}) should be regulated by

$$\frac{NU_{c1}I_{dc}}{6}=\frac{I_{j1}U_{j1}\cos(\varphi_1)}{2}$$
$$\frac{NU_{c3}I_{dc}}{6}=\frac{I_{j2}U_{j2}\cos(\varphi_2)}{2}. \quad (38)$$

The complete control scheme of the proposed 9A-MMC is illustrated in Fig. 9, which is mainly composed of the ac voltage control, capacitor voltage balancing control (CVBC), and circulating current suppression control (CCSC).

Among various modulation methods, phase-shifted carrier-based PWM (PSC-PWM) is adopted to generate switching signals for each SM. Under the PSC-PWM, each SM is controlled independently, and there are in total N, K, N triangular carriers with phase shifted by $2\pi/N$, π/K, $2\pi/N$ for the upper, middle and lower arms, respectively. Then, the comparisons between SM modulation references and triangular carriers produce the corresponding SM switching signals. The CVBC is usually separated into the average voltage control and the balancing voltage control, whose detailed description can be found in [26], and the block diagrams are shown in Fig. 10(a). The CCSC is implemented by several parallel quasi-PR controllers, where the circulating currents whose frequency below fifth order are considered. The detailed block diagram of CCSC in this article is shown in Fig. 10(b), and the transfer function of the quasi-PR controller is expressed as

$$G_{QPR\_n}(s)=K_p+\frac{2K_r\omega_c s}{s^2+2\omega_c s+(n\omega_0)^2} \quad (39)$$

where K_p and K_r are the proportional coefficient and gain of the corresponding order resonance, respectively; ω_c is used to increase the bandwidth around the resonant frequency; and ω_0 is the fundamental frequency. The detailed design processes of PI and PR controller parameters are shown in Appendix A and B, respectively.

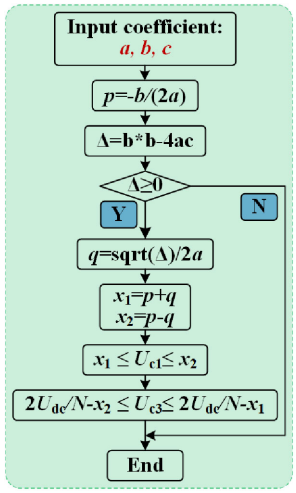

Fig. 8. Flowchart of calculation program about $\sqrt{A^2+B^2} \le I_{\rm dc}/3$.

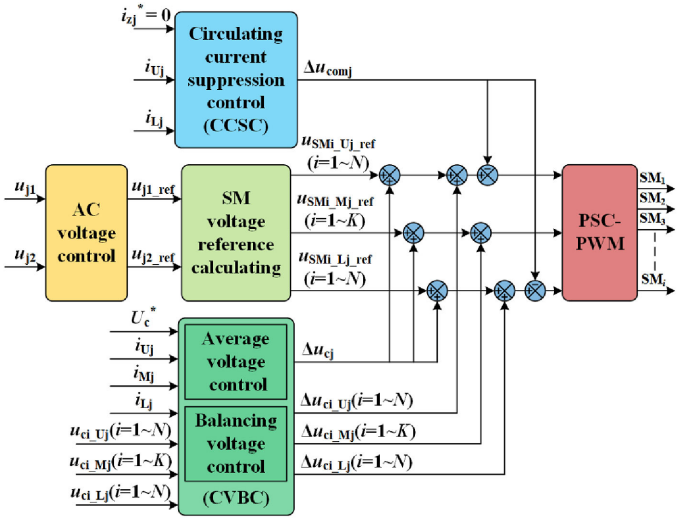

Fig. 9. Complete control scheme of the proposed 9A-MMC.

The compensation signals generated by CVBC and CCSC are added into the fundament modulation signals generated by the ac voltage control, whose detailed block diagram is shown in Fig. 10(c). It is noted that the control scheme is designed for powering two sets of loads, so the ac voltage regulation is applied to generate the fundament modulation signals. However, if the new 9A-MMC is connected into grid, the ac current controller will be used to generate the fundament modulation signals. Finally, the synthetic modulation signals are sent into the modulation stage. The final modulation reference signals for the *i*th SM in the upper, middle, and lower arms can be expressed

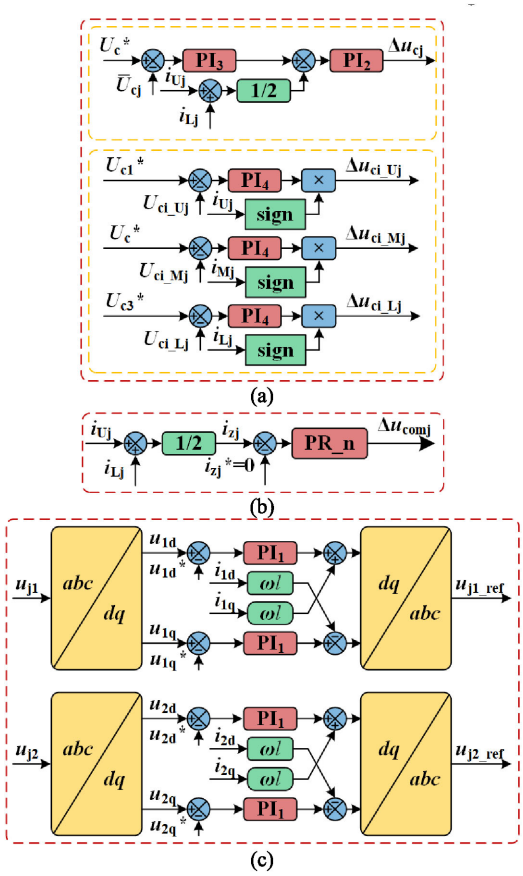

Fig. 10. Block diagrams of: (a) the capacitor voltage balancing control; (b) the circulating current suppression control; (c) the ac voltage control.

as

$$u_{\rm SMi\_Uj} = [1 - M_1 \sin(\omega t)]/2 + \Delta u_{\rm cj} + \Delta u_{\rm ci\_Uj} - \Delta u_{\rm comj} \tag{40}$$

$$u_{\rm SMi\_Mj} = \left[\frac{NU_{\rm c1}}{2KU_c} M_1 \sin(\omega t) - \frac{NU_{\rm c3}}{2KU_c} M_2 \sin(\omega t + \theta)\right] + \Delta u_{\rm cj} + \Delta u_{\rm ci\_Mj} \tag{41}$$

$$u_{\rm SMi\_Lj} = [1 + M_2 \sin(\omega t + \theta)]/2 + \Delta u_{\rm cj} + \Delta u_{\rm ci\_Lj} - \Delta u_{\rm comj}. \tag{42}$$

V. Simulation Results

To verify the performance of the proposed 9A-MMC, the corresponding circuit is built in MATLAB/Simulink to power two sets of three-phase loads. The dc-side of 9A-MMC is connected to an ideal dc source. The corresponding design parameters are listed in Table II. The simulation results under three scenarios discussed in Section III are sequentially displayed.

$$\lambda = \frac{-NI_{\rm dc}[U_{\rm c3}\cos(\theta-\varphi_2)U_{j1} + U_{\rm c1}\cos(\varphi_2)U_{j2}] + 3U_{j1}U_{j2}\cos(\theta-\varphi_2)[\cos(\theta+\varphi_1)I_{j1} + \cos(\varphi_2)I_{j2}]}{3[\cos(\theta+\varphi_1)\cos(\theta-\varphi_2) - \cos(\varphi_1)\cos(\varphi_2)]I_{j1}U_{j1}U_{j2}} \tag{36}$$

$$\mu = \frac{-NI_{\rm dc}[U_{\rm c3}\cos(\varphi_1)U_{j1} + U_{\rm c1}\cos(\theta+\varphi_1)U_{j2}] + 3U_{j1}U_{j2}\cos(\theta+\varphi_1)[\cos(\varphi_1)I_{j1} + \cos(\theta-\varphi_2)I_{j2}]}{3[\cos(\theta+\varphi_1)\cos(\theta-\varphi_2) - \cos(\varphi_1)\cos(\varphi_2)]I_{j2}U_{j1}U_{j2}} \tag{37}$$

TABLE II
THE DESIGN PARAMETERS OF PROPOSED 9A-MMC

Parameters	Values
Initial SM capacitor voltage U_c	1kV
SM capacitor C_{sm}	2mF
Fundamental frequency f_0	50Hz
Carrier frequency f_c	5kHz
Arm inductor L_{arm}	5mH
Output filter inductor L	5mH
Loads resistance R	30Ω
DC-side voltage U_{dc}	4kV
SM number N	4

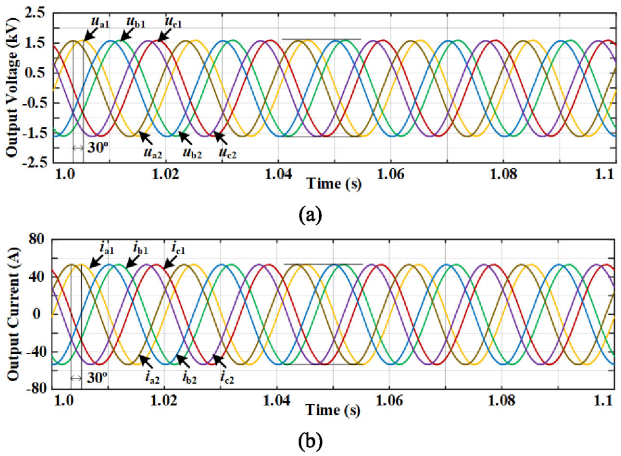

Fig. 11. (a) Output voltages of upper and lower terminals. (b) Output currents of the upper and lower terminals.

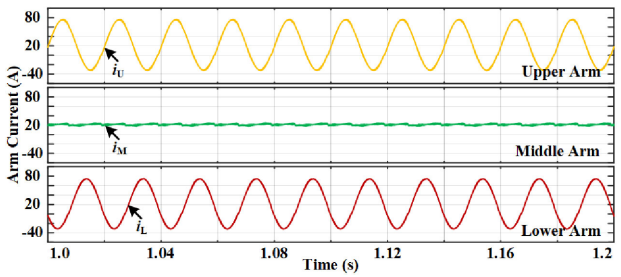

Fig. 12. Upper, middle, and lower arm currents in phase A.

Case 1: $\sqrt{A^2+B^2}=0$, $u_{j1}=1.6\,\text{kV}$ ($M_1=0.8$), $u_{j2}=1.6\,\text{kV}$ ($M_2=0.8$), $\theta=30°$

The first scenario is that both M_1 and M_2 are set as 0.8 and θ is set as 30°. Under this scenario, λ and μ are equal to 1, and there is only the dc component in the middle arm current.

The upper and lower output voltages (u_{a1}, u_{b1}, u_{c1} and u_{a2}, u_{b2}, u_{c2}) and currents (i_{a1}, i_{b1}, i_{c1} and i_{a2}, i_{b2}, i_{c2}) are shown in Fig. 11(a) and (b), respectively. It is clear that the upper and lower output voltages and currents are standard sinusoidal waveforms. The upper, middle, and lower arm currents (i_U, i_M, and i_L) are presented in Fig. 12, the middle arm current is only composed of the dc component, and the upper output current only flows through the upper arm, the lower output current only flows through the lower arm. This is consistent with the analyses in Section III. Fig. 13 displays the SM capacitor voltages in the upper, middle, and lower arms (u_{c_U}, u_{c_M}, and u_{c_L}), and all the

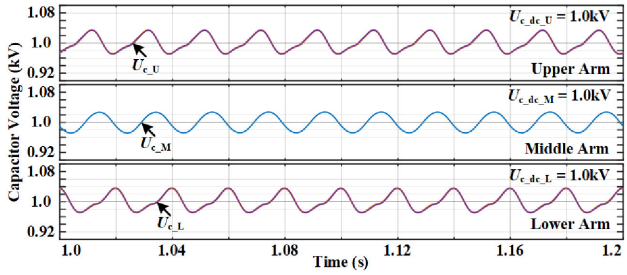

Fig. 13. SM capacitor voltages in the upper, middle, and lower arm.

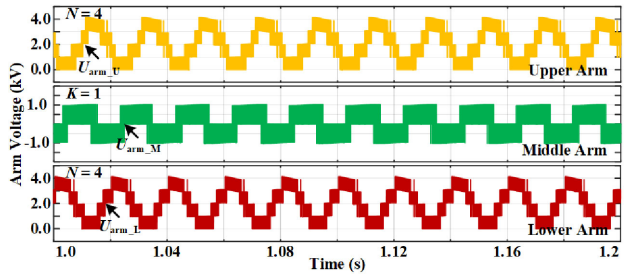

Fig. 14. Upper, middle, and lower arm voltage levels with $N=4$, $K=1$.

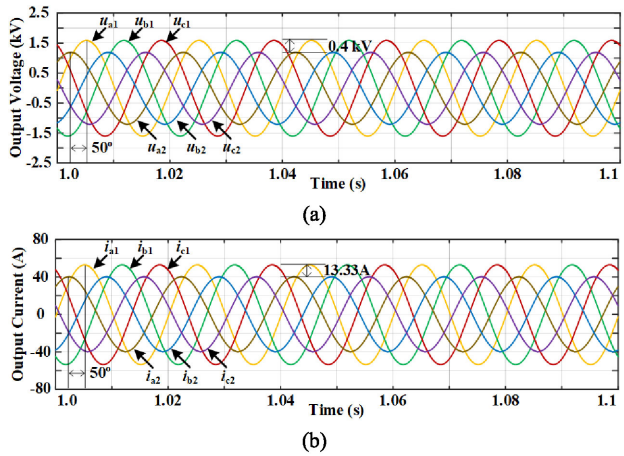

Fig. 15. (a) Output voltages of the upper and lower terminal. (b) Output currents of the upper and lower terminal.

SM capacitor voltages are balanced at 1.0 kV as expected. Fig. 14 presents the upper, middle, and lower arm switching voltages ($u_{\text{arm\_U}}$, $u_{\text{arm\_M}}$, and $u_{\text{arm\_L}}$). It can be seen that because the upper and lower arms are formed by the HBSMs and the middle arms are formed by the UC-FBSMs, the upper and lower arm voltages shown in Fig. 14 are always positive, while the middle arm voltages are bidirectional. Moreover, only one UC-FBSM is required in the middle arm under the first scenario.

Case 2: $\sqrt{A^2+B^2}\le I_{\text{dc}}/3$, $u_{j1}=1.6\,\text{kV}$ ($M_1=0.8$), $u_{j2}=1.2\,\text{kV}$ ($M_2=0.6$), $\theta=50°$

The second scenario is that M_1 and M_2 are 0.8 and 0.6, θ is 50°. The amplitude of the ac component in the middle arm current is smaller than the dc component under this scenario, and the middle arm current is still positive.

Fig. 15(a) records (u_{a1}, u_{b1}, u_{c1}) and (u_{a2}, u_{b2}, u_{c2}), while Fig. 15(b) shows (i_{a1}, i_{b1}, i_{c1}) and (i_{a2}, i_{b2}, i_{c2}). It is shown

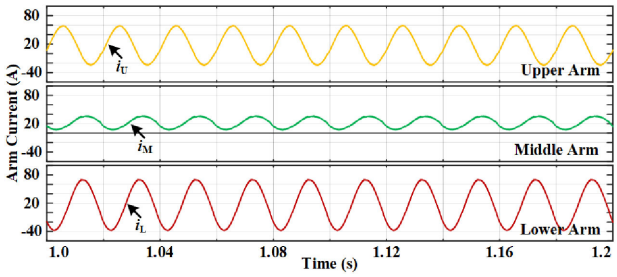

Fig. 16. Upper, middle, and lower arm currents in phase A.

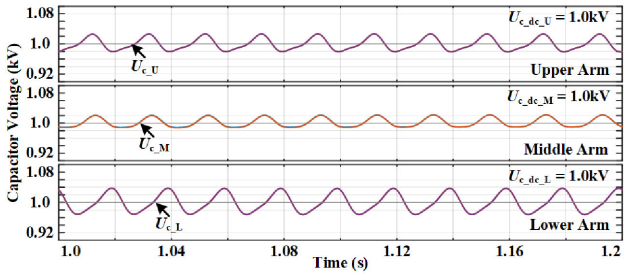

Fig. 17. SM capacitor voltages in the upper, middle, and lower arm.

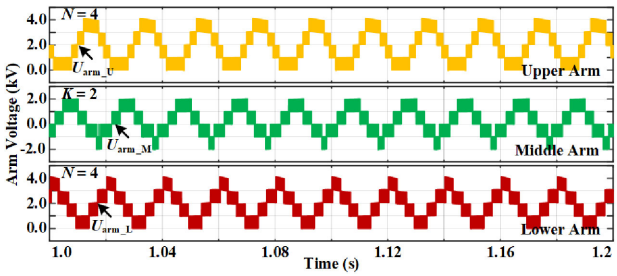

Fig. 18. Upper, middle, and lower arm voltage levels with $N = 4$ and $K = 2$.

that the proposed 9A-MMC can also output satisfied waveforms under this scenario. i_U, i_M, and i_L are presented in Fig. 16, where i_M is always positive. $u_{\mathrm{c\_U}}$, $u_{\mathrm{c\_M}}$, and $u_{\mathrm{c\_L}}$ are shown in Fig. 17. All the SM capacitor voltages can be balanced around the SM capacitor voltage reference 1.0 kV. $u_{\mathrm{arm\_U}}$, $u_{\mathrm{arm\_M}}$, and $u_{\mathrm{arm\_L}}$ are presented in Fig. 18, it is shown that two UC-FBSMs are required in the middle arm under this scenario.

Case 3: $\sqrt{A^2 + B^2} > I_{\mathrm{dc}}/3$, $u_{j1} = 1.6\,\mathrm{kV}$ ($M_1 = 0.8$), $u_{j2} = 1.2\,\mathrm{kV}$ ($M_2 = 0.6$), $\theta = 80°$

The third scenario is that M_1 and M_2 are still set as 0.8 and 0.6, but θ is enlarged to 80°. Under this scenario, the amplitude of the ac component in the middle arm current is larger than the dc component, and the middle arm current is bidirectional. The proposed 9A-MMC cannot directly operate under this scenario. Therefore, the middle arm current reshaping control method is employed to ensure the middle arm current to be positive. According to the proposed middle arm reshaping control method shown in Fig. 7, the SM capacitor voltages of the upper and lower arms under this scenario are adjusted to be 1.05 and 0.95 kV, respectively.

(u_{a1}, u_{b1}, u_{c1}) and (u_{a2}, u_{b2}, u_{c2}) are shown in Fig. 19(a), and (i_{a1}, i_{b1}, i_{c1}) and (i_{a2}, i_{b2}, i_{c2}) are shown in Fig. 19(b). Fig. 20

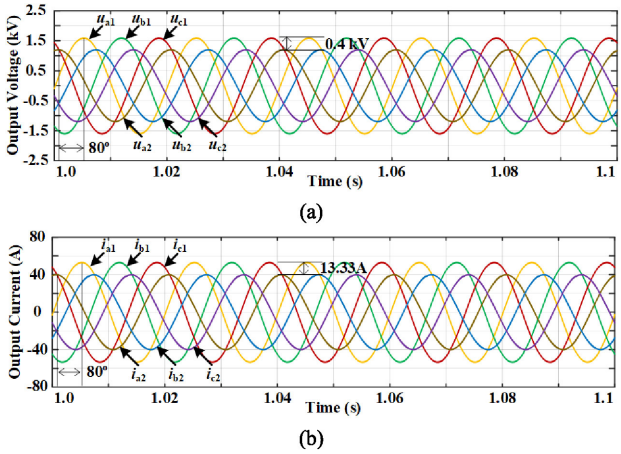

Fig. 19. (a) Output voltages of the upper and lower terminal. (b) Output currents of the upper and lower terminal.

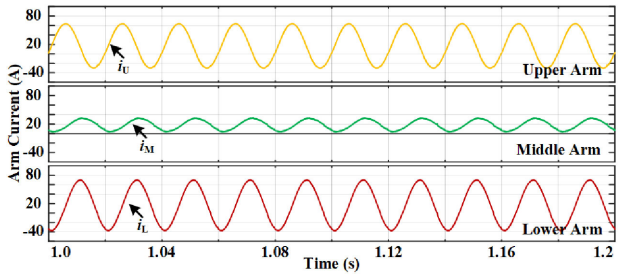

Fig. 20. Upper, middle, and lower arm currents in phase A.

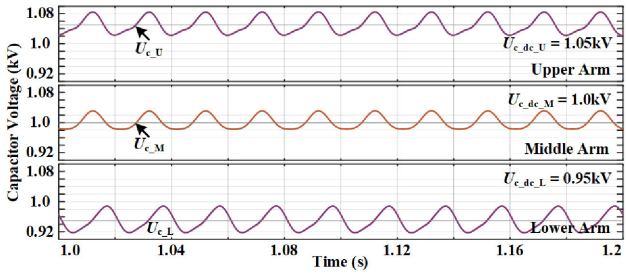

Fig. 21. SM capacitor voltages in the upper, middle, and lower arms.

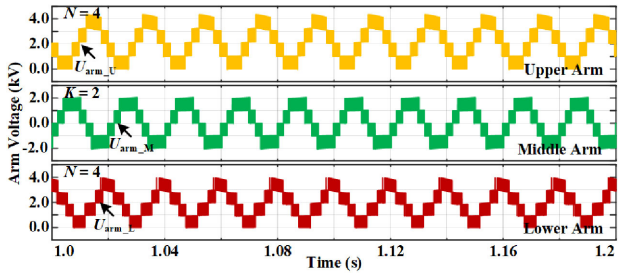

Fig. 22. Upper, middle, and lower arm voltage levels with $N = 4$ and $K = 2$.

presents i_U, i_M, and i_L, and i_M can be always positive with the proposed middle arm current reshaping control method. $u_{\mathrm{c\_U}}$, $u_{\mathrm{c\_M}}$, and $u_{\mathrm{c\_L}}$ are presented in Fig. 21. It can be seen that $u_{\mathrm{c\_U}}$ and $u_{\mathrm{c\_L}}$ are balanced around 1.05 and 0.95 kV, respectively, $u_{\mathrm{c\_M}}$ is balanced around 1.0 kV. Fig. 22 shows $u_{\mathrm{arm\_U}}$, $u_{\mathrm{arm\_M}}$, and $u_{\mathrm{arm\_L}}$. It is revealed that the proposed middle arm current

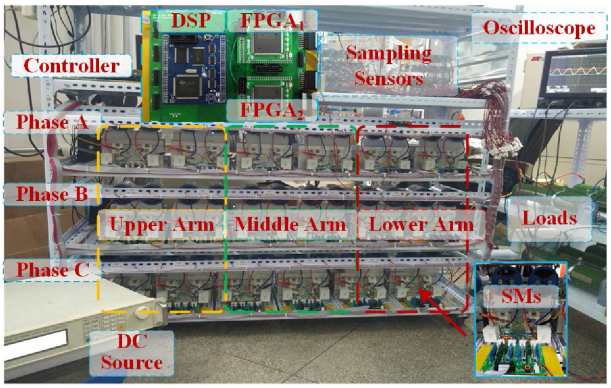

Fig. 23. Photograph of the proposed three-phase 9A-MMC prototype.

TABLE III
EXPERIMENTAL PARAMETERS OF PROPOSED 9A-MMC

Parameters		Values
Initial SM capacitor voltage		50V
SM capacitor	Upper and lower arm	2mF
	Middle arm	1.04mF
Fundamental frequency		50Hz
Carrier frequency		5kHz
Arm inductor		2mH
Output filter inductor		5mH
Loads resistance		30Ω
DC-side voltage		200V
SM number		4

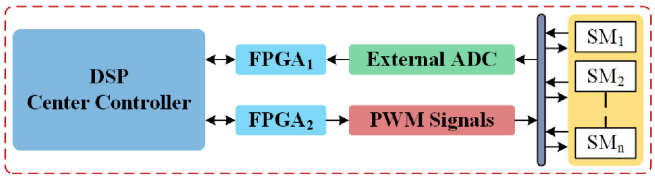

Fig. 24. Structure of the control system.

reshaping control method can guarantee the middle arm current to be always positive.

VI. EXPERIMENTAL RESULTS

As shown in Fig. 23, a scale-down three-phase prototype has been built to further validate the performance of the proposed 9A-MMC. The experimental parameters are listed in Table III. The whole control scheme is implemented in a controller consisting of a TMS320F28335 digital signal processor (DSP) plus two XC3S500E-4PQG208C field programmable gate arrays (FPGAs). The DSP is used to read the external analog-to-digital converter (ADC) results and perform most of the calculation. Finally, it will provide the modulation reference for each SM. Meanwhile, one FPGA is used to control the external ADC to obtain the arm currents, SM capacitor voltages, and output voltages and currents, and the other FPGA is used to carry out the modulation and send switching signals to each SM. The detailed structure of the control system is shown in Fig. 24.

The experimental results under the first scenario are shown in Fig. 25, where both M_1 and M_2 are set as 0.7 and θ is 80°.

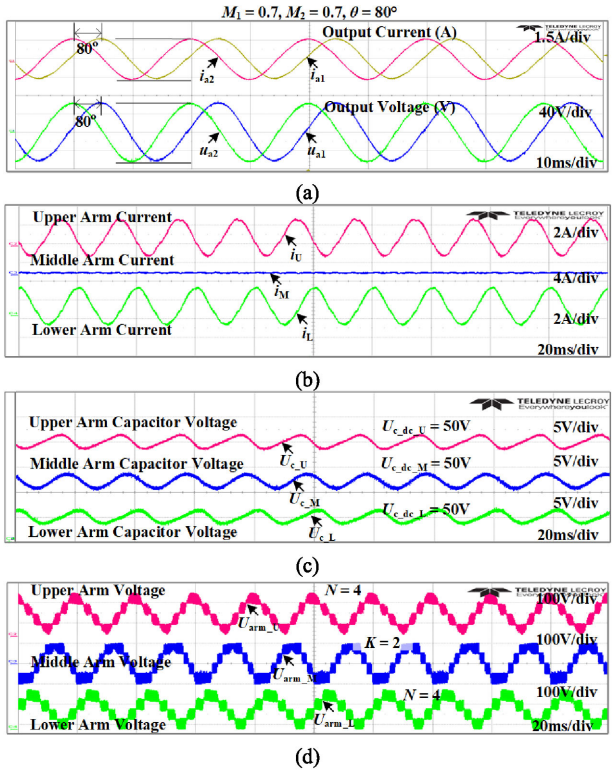

Fig. 25. Experimental results of (a) upper and lower output voltages and currents in phase A, (b) three arm currents, (c) SM capacitor voltages in three arms, and (d) three arm voltage levels under the first scenario.

In specific, the upper and lower output voltages and currents in phase A (u_{a1}, u_{a2}, and i_{a1}, i_{a2}) are shown in Fig. 25(a). The upper, middle, and lower arm currents (i_U, i_M, and i_L) are displayed in Fig. 25(b), it can be seen that the middle arm current only consists of the dc component. Fig. 25(c) presents the SM capacitor voltages in the upper, middle, and lower arms ($u_{\mathrm{c\_U}}$, $u_{\mathrm{c\_M}}$, and $u_{\mathrm{c\_L}}$), all the SM capacitor voltages can be balanced around the SM capacitor voltage reference. Fig. 25(d) shows the upper, middle, and lower arm voltage levels ($u_{\mathrm{arm\_U}}$, $u_{\mathrm{arm\_M}}$, and $u_{\mathrm{arm\_L}}$).

Fig. 26 presents (u_{a1}, u_{a2}, and i_{a1}, i_{a2}), (i_U, i_M, and i_L), ($u_{\mathrm{c\_U}}$, $u_{\mathrm{c\_M}}$, and $u_{\mathrm{c\_L}}$), and ($u_{\mathrm{arm\_U}}$, $u_{\mathrm{arm\_M}}$, and $u_{\mathrm{arm\_L}}$) under the second scenario, where M_1 and M_2 are set as 0.8 and 0.7 and θ is 60°. Under this scenario, the middle arm current contains the ac component except for the dc component, but the amplitude of the ac component is smaller than the dc component, the middle arm current is still positive. There is no need to adopt the proposed middle arm current reshaping control method.

The experimental results under the third scenario are shown in Fig. 27(a)–(d), where M_1 and M_2 are 0.8 and 0.6 and θ is 70°. The middle arm current reshaping control method is adopted to ensure the middle arm current to be always positive. According to Fig. 7, the SM capacitor voltages of upper and lower arms are adjusted to 52 and 48 V, respectively. As shown in Fig. 27(b), the middle arm current becomes to be positive. It can be seen from Fig. 27(c) that the SM capacitor voltages in the upper and lower arms are balanced around 52 and 48 V, the SM capacitor voltage

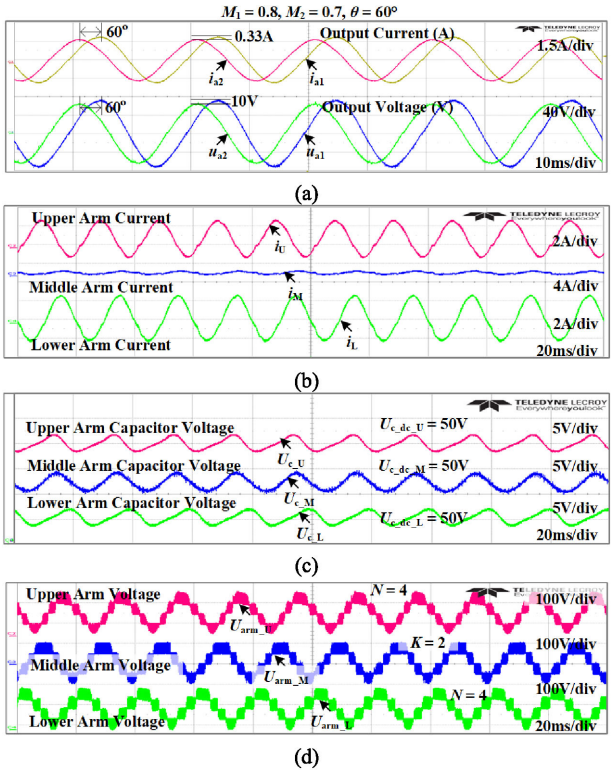

Fig. 26. Experimental results of (a) upper and lower output voltages and currents in phase A, (b) three arm currents, (c) SM capacitor voltages in three arms, and (d) three arm voltage levels under the second scenario.

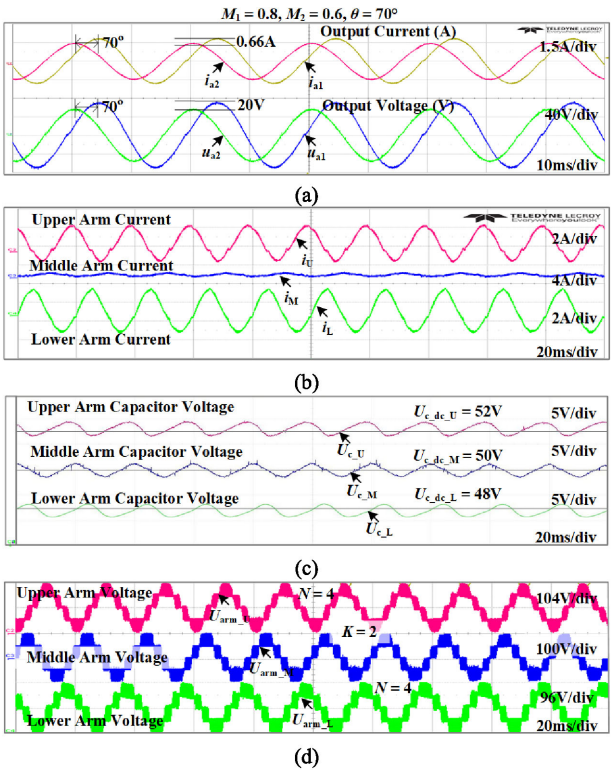

Fig. 27. Experimental results of (a) upper and lower output voltages and currents in phase A, (b) three arm currents, (c) SM capacitor voltages in three arms, (d) three arm voltage levels under the third scenario.

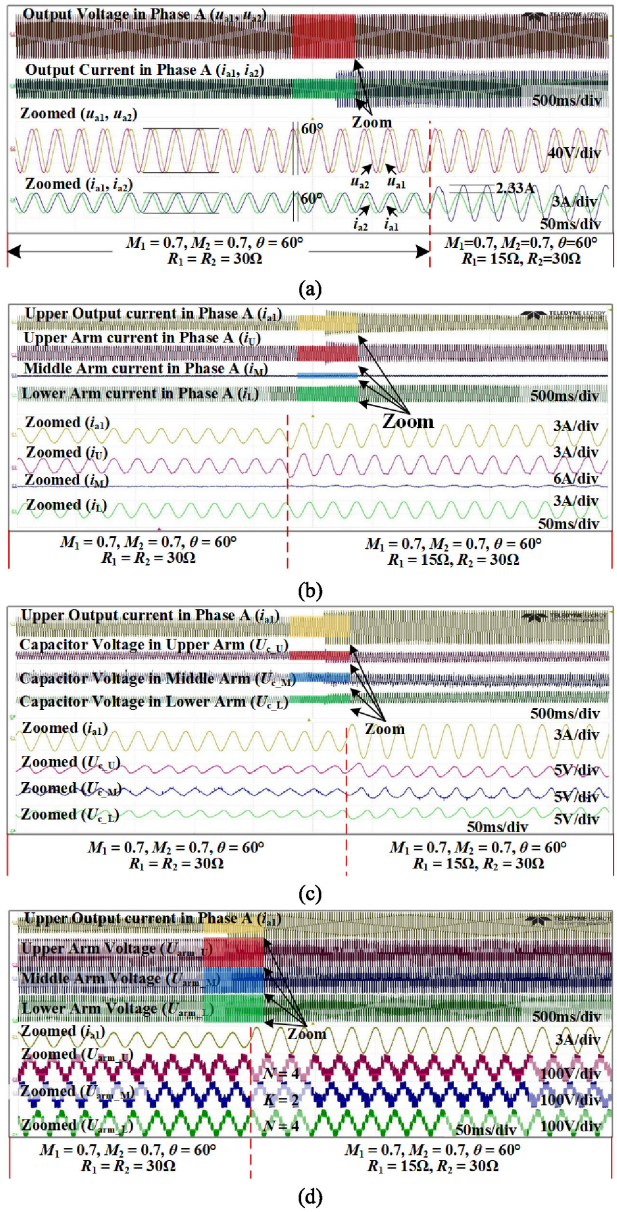

Fig. 28. Experimental results of (a) upper and lower output voltages and currents in phase A, (b) three arm currents, (c) SM capacitor voltages in three arms, and (d) three arm voltage levels when the upper load changes.

in the middle arm is balanced around the initial SM capacitor voltage reference 50 V. As shown in Figs. 25(d), 26(d), and 27(d), two UC-FBSMs are required in the middle arm under the above three scenarios.

To evaluate the dynamic performances of the proposed 9A-MMC, the step change of loads or modulation indexes is implemented. When changing load, both M_1 and M_2 are set as 0.7 and θ is set as 60°. The experimental results including (u_{a1}, u_{a2}, and i_{a1}, i_{a2}), (i_U, i_M, and i_L), (u_{c_U}, u_{c_M}, and u_{c_L}), and (u_{arm_U}, u_{arm_M}, and u_{arm_L}) when the upper load changes from 30 to 15 Ω, but the lower load is unchanged, as shown in Fig. 28(a)–(d). Fig. 29 shows the experimental results when M_1 changes from 0.6 to 0.8, and M_2 and θ are kept at 0.6 and 60°,

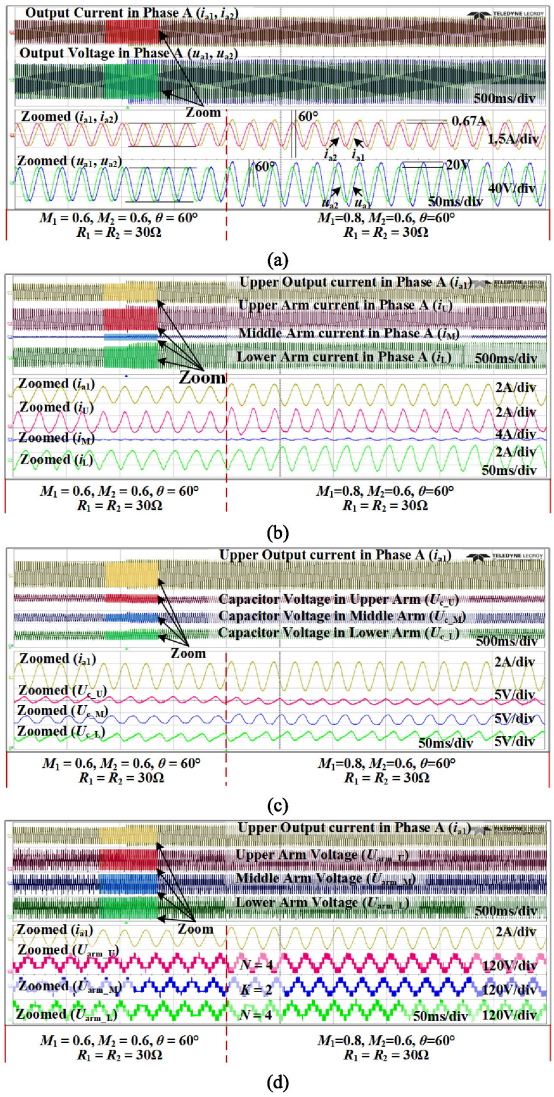

Fig. 29. Experimental results of (a) upper and lower output voltages and currents in phase A, (b) three arm currents, (c) SM capacitor voltages in three arms, and (d) three arm voltage levels when M_1 changes.

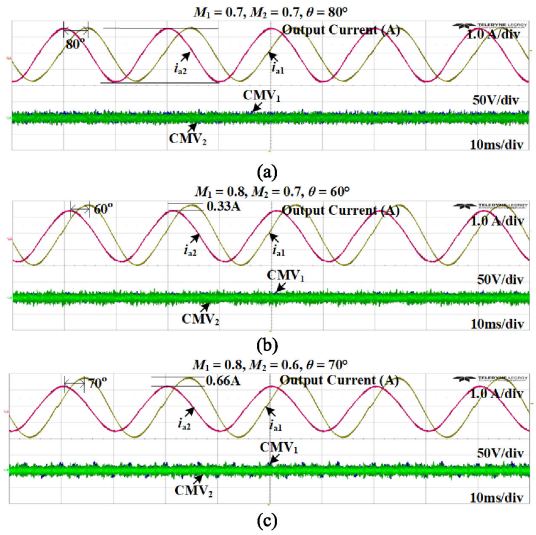

Fig. 30. Common mode voltage in the upper and lower output terminals under three different operation conditions.

respectively. Besides, the CMVs in the upper and lower output terminals under three different operation conditions are shown in Fig. 30 (a)–(c), respectively. It can be seen that there is no dc offset in the CMVs of the new 9A-MMC.

VII. Conclusion

In this article, a new 9A-MMC with the improved hybrid submodules has been proposed, where the upper and lower arms are formed by the half-bridge submodules (HBSMs), the middle arms are formed by the unidirectional current full-bridge submodules (UC-FBSMs). The complete operation analysis of the proposed 9A-MMC including the actually required submodules count in the middle arm and the three scenarios of the middle arm current have been discussed in detail. Because the new 9A-MMC cannot directly operate when the middle arm current is bidirectional. This article, therefore, proposes a middle arm current reshaping control method, which can shift the bidirectional middle arm current to be always positive. Compared with the standard 9A-MMC, the dc-side voltage of the new 9A-MMC can be reduced by 1/3, and the switch count of the new 9A-MMC is the same as that of the standard 9A-MMC. Moreover, the dc offset of CMV is fully eliminated. Finally, simulation and experimental results verified the performance of the proposed 9A-MMC and the effectiveness of the developed middle arm current reshaping control method.

Appendix A

The control diagram of the d-axis control of the upper output terminal is shown in Fig. 31 (a), where $G_{c1}(s)$ represents the transfer function of the PI_1 controller in which k_{p1} and τ_{i1} are the tuned parameters. $G_{\mathrm{PWM}}(s)$ is the transfer function of the modulator in which K_{PWM} is the equivalent gain and T_s is the time constant of PWM module. $H(s)$ denotes the transfer function of the sampling and digital processing in which T_d is the time delay caused by them. L_{eq} and R_{eq} are, respectively, the equivalent inductance and resistance of the ac-side. The open loop transfer function of the PI_1 control process can be expressed as follows:

$$\begin{aligned} G_{\mathrm{op1}}(s) &= NU_c G_{\mathrm{c1}}(s) G_{\mathrm{PWM}}(s) G_{\mathrm{circuit1}}(s) H(s) \\ &= NU_c \cdot \frac{k_{\mathrm{p1}}(\tau_{i1}s+1)}{\tau_{i1}s} \cdot \frac{K_{\mathrm{PWM}}}{T_s s+1} \cdot \frac{1}{L_{\mathrm{eq}}s+R_{\mathrm{eq}}} \\ &\quad \cdot \frac{1}{T_d s+1}. \end{aligned} \tag{A-1}$$

Since T_s and T_d are both small enough, the second and the last terms can be merged as follows, where $T_m = T_s + T_d$:

$$\frac{K_{\mathrm{PWM}}}{T_m s+1} = \frac{K_{\mathrm{PWM}}}{T_s s+1} \cdot \frac{1}{T_d s+1}. \tag{A-2}$$

Considering the fast response of the ac voltage control, its parameters can be tuned according to the parameters tuning principle of the typical Type I system. If choosing $\tau_{i1} = L_{\mathrm{eq}}/R_{\mathrm{eq}}$, the open loop transfer function of (A-1) can be adjusted as follows:

$$\begin{cases} G_{\mathrm{op1}}(s) = \frac{K_1}{s(T_m s+1)} \\ K_1 = \frac{NU_c k_{\mathrm{p1}} K_{\mathrm{PWM}}}{R_{\mathrm{eq}} \tau_{i1}}. \end{cases} \tag{A-3}$$

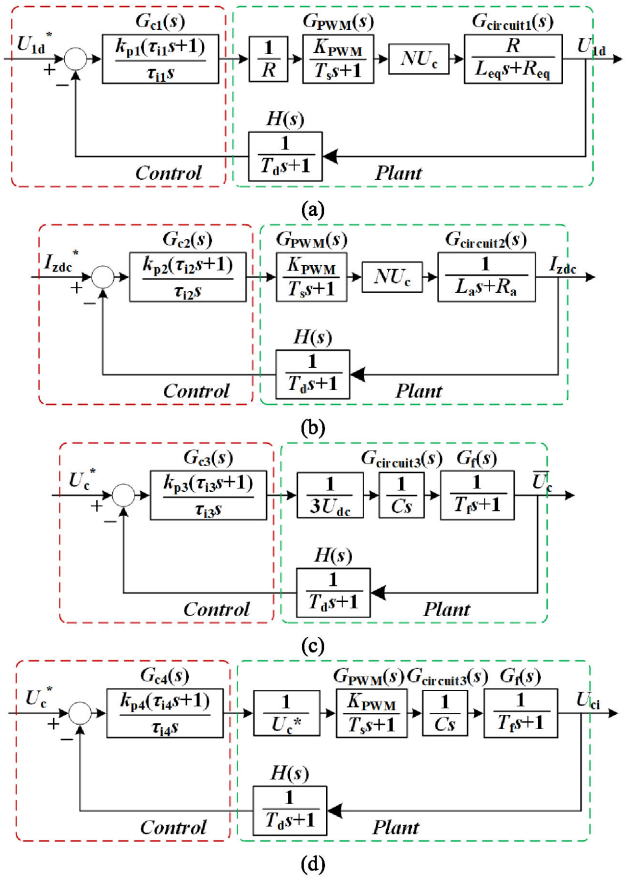

Fig. 31. Control diagram of (a) the ac voltage control, (b) the inner current control in the average voltage control, (c) the outer voltage control in the averaging voltage control, and (d) the balancing capacitor voltage control.

The close loop transfer function of (A-3) can be derived as follows:

$$G_{c1}(s)=\frac{G_{op1}(s)}{1+G_{op1}(s)}=\frac{\frac{K_1}{T_m}}{s^2+\frac{1}{T_m}s+\frac{K_1}{T_m}}. \tag{A-4}$$

According to the parameters tuning principle of the typical Type I system, the damping ratio ξ is chosen as 0.707

$$\xi=\frac{1}{2\sqrt{\frac{NU_c k_{p1}K_{PWM}T_m}{R_{eq}\tau_{i1}}}}=0.707 \tag{A-5}$$

Therefore, the parameters of the PI_1 controller in the AC voltage control can be expressed as follows:

$$\begin{cases} k_{p1}=\frac{R_{eq}\tau_{i1}}{2NU_cT_mK_{PWM}} \\ \tau_{i1}=\frac{L_{eq}}{R_{eq}}. \end{cases} \tag{A-6}$$

The control diagram of the inner current control loop in the average voltage control is shown in Fig. 31(b). The PI_2 controller are also tuned according to parameters tuning principle of the typical Type I system, and the design process is similar to that of the PI_1 controller. The parameters (k_{p2}, τ_{i2}) can be expressed as follows:

$$\begin{cases} k_{p2}=\frac{R_a\tau_{i2}}{2NU_cT_mK_{PWM}} \\ \tau_{i2}=\frac{L_a}{R_a} \end{cases} \tag{A-7}$$

where L_a and R_a are, respectively, the equivalent inductance and resistance of the arm.

TABLE IV
PARAMETERS OF CONTROLLERS

Parameters	Value
k_{p1}, τ_{i1}	0.0125, 0.05
k_{p2}, τ_{i2}	0.008, 0.05
k_{p3}, τ_{i3}	180, 0.2
k_{p4}, τ_{i4}	15, 0.2
K_p, ω_c	0.00278, 5
K_{r2}, K_{r3}, K_{r4}	0.23, 0.32, 0.452

Because the cut-off frequency of the outer voltage control loop in the average voltage control is much smaller than that of the inner current control loop, the inner current control loop can be regarded as the unit 1 when the parameters of the outer voltage control loop are designed. The control diagram of the outer voltage control loop is shown in Fig. 31(c), where $G_f(s)$ denotes the transfer function of the low pass filter in which T_f is the time delay caused by the filter. Considering the anti-interference ability of the capacitor voltage control, the parameters of PI_3 controller can be tuned according to the parameters tuning principle of the typical Type II system. The open loop transfer function of the outer voltage control is expressed as follows:

$$\begin{aligned} G_{op3}(s)&=\frac{1}{3U_{dc}}G_{c3}(s)G_f(s)G_{circuit3}(s)H(s) \\ &=\frac{k_{p3}}{3U_{dc}\tau_{i3}C}\cdot\frac{(\tau_{i3}s+1)}{s^2(T_fs+1)}\cdot\frac{1}{T_ds+1}. \end{aligned} \tag{A-8}$$

Because $T_ds<<1$, the open loop transfer function of (A-8) can be simplified as follows:

$$\begin{cases} G_{op3}(s)=\frac{K_2(\tau_{i3}s+1)}{s^2(T_fs+1)} \\ K_2=\frac{k_{p3}}{3U_{dc}\tau_{i3}C}. \end{cases} \tag{A-9}$$

Based on the design rules of typical Type II system, the parameters (K_2, τ_{i3}) can be obtained as follows:

$$\begin{cases} K_2=\frac{h+1}{2h^2T_f^2} \\ \tau_{i3}=hT_f \end{cases} \tag{A-10}$$

where h is selected as 5, and $T_f = 40$ ms. Then, k_{p3} can be obtained.

The control diagram of the balancing voltage control is shown in Fig. 31(d), the parameters of PI_4 controller are also tuned according to the design rules of typical Type II system. The simplified open loop transfer function is expressed as follows:

$$\begin{cases} G_{op4}(s)=\frac{K_3(\tau_{i4}s+1)}{s^2(T_fs+1)} \\ K_3=\frac{k_{p4}}{U_c\tau_{i4}C}. \end{cases} \tag{A-11}$$

Finally, the parameters (K_3, τ_{i4}) of PI_4 controller can be obtained as follows:

$$\begin{cases} K_3=\frac{h+1}{2h^2T_f^2} \\ \tau_{i4}=hT_f. \end{cases} \tag{A-12}$$

The specific parameters of the PI controllers in Fig. 10 are summarized in Table IV.

APPENDIX B

Fig. 32(a) shows the control diagram of the second-order circulating current suppression control, and the open loop transfer

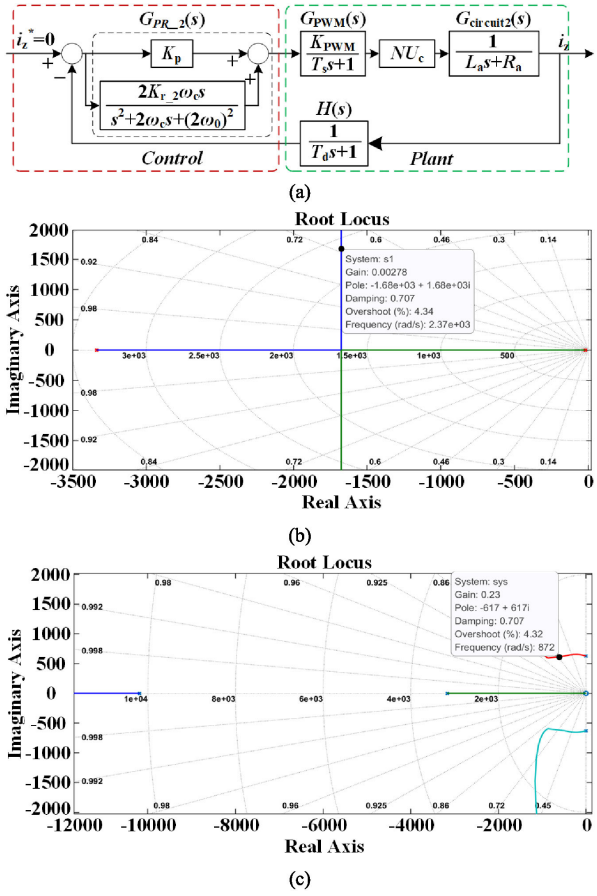

Fig. 32. (a) Control diagram of the second-order circulating current suppression control, (b) the root locus of (B-2), and (c) the root locus of (B-3).

function of the PR_2 control process is expressed as follows:

$$G_{\mathrm{op5}}(s) = NU_c G_{\mathrm{PR\_2}}(s) G_{\mathrm{PWM}}(s) G_{\mathrm{circuit2}}(s) H(s) = \frac{\frac{NU_c K_p K_{\mathrm{PWM}}}{T_m L_0} \cdot (s^2 + 2\omega_c(1+\frac{K_{\mathrm{r2}}}{K_p})s + 4\omega_0^2)}{(s^2+2\omega_c s+4\omega_0^2)(s+\frac{1}{T_m})(s+\frac{R_0}{L_0})}. \tag{B-1}$$

To determine the proportional gain of the controller, the open loop transfer function can be redefined for $K_{\mathrm{r2}} = 0$, leading to

$$G_{\mathrm{op5}}(s) = \frac{K_p \cdot \frac{NU_c K_{\mathrm{PWM}}}{T_m L_0}}{(s+\frac{1}{T_m})(s+\frac{R_0}{L_0})}. \tag{B-2}$$

According to (B-2) and the circuit parameters shown in Table II, the root locus of (B-2) can be shown in Fig. 32(b). If the damping factor is about 0.707, $K_p = 0.00278$.

The equation of root locus of (B-1) can be expressed as follows:

$$\begin{aligned} G^*{}_{\mathrm{op5}}(s) = & \frac{2K_{\mathrm{r2}} NU_c K_{\mathrm{PWM}} \omega_c s}{[T_m L_0 s^4 + (T_m R_0 + L_0 + 2T_m L_0 \omega_c)s^3} \\ & + (NU_c K_p K_{\mathrm{PWM}} + R_0 + 4T_m L_0 \omega_0^2 \\ & + 2(T_m R_0 + L_0)\omega_c)s^2 + (4(T_m R_0 + L_0)\omega_0^2 \\ & + 2(NU_c K_p K_{\mathrm{PWM}} + R_0)\omega_c)s \\ & + 4(NU_c K_p K_{\mathrm{PWM}} + R_0)\omega_0^2] \\ = & -1. \end{aligned} \tag{B-3}$$

Besides, $\omega_c = 2\pi\Delta f$, if the error of frequency is 0.5Hz, $\omega_c = \pi$. Then, substituting $K_p = 0.00278$ into (B-3), the root locus of (B-3) can be shown in Fig. 32(c). If the damping factor is selected as 0.707, $K_{\mathrm{r2}} = 0.23$. The parameters of the PR controllers for the third- and fourth-order circulating current suppression can also be tuned according to the above deduction, and the corresponding parameters are summarized in Table IV.

REFERENCES

[1] R. Marquardt and A. Lesnicar, "A new modular voltage source inverter topology," in *Proc. Eur. Power Electron. Conf.*, 2003, pp. 1–10.

[2] A. Lesnicar and R. Marquardt, "An innovative modular multilevel converter topology suitable for a wide power range," in *Proc. IEEE Power Tech. Conf.*, 2003, vol. 3, pp. 1–6.

[3] M. Saeedifard and R. Iravani, "Dynamic performance of a modular multilevel back-to-back HVDC system," *IEEE Trans. Power Del.*, vol. 25, no. 4, pp. 2903–2912, Oct. 2010.

[4] A. Nami, J. Liang, F. Dijkhuizen, and G. D. Demetriades, "Modular multilevel converters for HVDC applications: Review on converter cells and functionalities," *IEEE Trans. Power Electron.*, vol. 30, no. 1, pp. 18–36, Jan. 2015.

[5] M. Guan and Z. Xu, "Modeling and control of a modular multilevel converter-based HVDC system under unbalanced grid conditions," *IEEE Trans. Power Electron.*, vol. 27, no. 12, pp. 4858–4867, Dec. 2012.

[6] X. Liu, J. Lv, C. Gao, Z. Chen, and S. Chen, "A novel STATCOM based on diode-clamped modular multilevel converters," *IEEE Trans. Power Electron.*, vol. 32, no. 8, pp. 5964–5977, Aug. 2017.

[7] H. P. Mohammadi and M. T. H. Bina, "A transformerless medium-voltage STATCOM topology based on extended modular multilevel converters," *IEEE Trans. Power Electron.*, vol. 26, no. 5, pp. 1534–1545, May 2011.

[8] Q. Hao, J. Man, F. Gao, and M. Guan, "Voltage limit control of modular multilevel converter based unified power flow controller under unbalanced grid conditions," *IEEE Trans. Power Del.*, vol. 33, no. 3, pp. 1319–1327, Jun. 2018.

[9] B. Tai, C. Gao, X. Liu, and Z. Chen, "A novel flexible capacitor voltage control strategy for variable-speed drives with modular multilevel converters," *IEEE Trans. Power Electron.*, vol. 32, no. 1, pp. 128–141, Jan. 2017.

[10] B. Li, S. Zhou, D. Xu, S. J. Finney, and B. W. Williams, "A hybrid modular multilevel converter for medium-voltage variable-speed motor drives," *IEEE Trans. Power Electron.*, vol. 32, no. 6, pp. 4619–4630, Jun. 2017.

[11] M. A. Perez, S. Bernet, J. Rodriguez, S. Kouro, and R. Lizana, "Circuit topologies, modeling, control schemes and applications of modular multilevel converters," *IEEE Trans. Power Electron.*, vol. 30, no. 1, pp. 4–17, Mar. 2014.

[12] A. Dekka, B. Wu, R. L. Fuentes, M. Perez, and N. R. Zargari, "Evolution of topologies, modeling, control schemes, and applications of modular multilevel converters," *IEEE J. Emerg. Sel. Top. Power Electron.*, vol. 5, no. 4, pp. 1631–1656, Dec. 2017.

[13] S. Debnath, J. Qin, B. Bahrani, M. Saeedifard, and P. Barbosa, "Operation, control, and applications of the modular multilevel converter: A review," *IEEE Trans. Power Electron.*, vol. 30, no. 1, pp. 37–53, Jan. 2015.

[14] Y. S. Kumar and G. Poddar, "Control of medium-voltage AC motor drive for wide speed range using modular multilevel converter," *IEEE Trans. Ind. Electron.*, vol. 64, no. 4, pp. 2742–2749, Apr. 2017.

[15] A. A. Elserougi, A. S. Abdel-Khalik, A. M. Massoud, and S. Ahmed, "A nine-arm modular multilevel converter (9A-MMC) for six-phase medium voltage motor drives," in *Proc. IEEE-IECON*, 2015, pp. 1735–1740.

[16] A. A. Elserougi, A. S. Abdel-Khalik, A. M. Massoud, and S. Ahmed, "An asymmetrical six-phase induction motor drive based on nine-arm modular multilevel converter (9AMMC) with circulating current suppression," in *Proc. IEEE-EPECS*, 2015, pp. 1–6.

[17] M. S. Diab, G. P. Adam, B. W. Williams, A. M. Massoud, and S. Ahmed, "Quasi two-level PWM operation of a nine-arm modular multilevel converter for six-phase medium-voltage motor drives," in *Proc. IEEE-APEC*, 2018, pp. 1641–1648.

[18] F. Qin, F. Gao, T. Xu, D. Niu, and Z. Ma, "A unified power flow controller with nine-arm modular multilevel converter," in *Proc. IEEE-ECCE*, 2018, pp. 2581–2587.

[19] J. Fu, B. Zhang, and D. Qiu, "A novel nine-arm modular multilevel converter," in *Proc. IEEE-IECON*, 2014, pp. 4528–4533.
[20] F. Qin, F. Gao, T. Xu, D. Niu, and Z. Ma, "A control scheme of nine-arm modular multilevel converter," in *Proc. IEEE-ECCE*, 2018, pp. 2143–2148.
[21] F. Qin, F. Gao, and C. Zhang, "Operational analyses and control scheme of nine-arm modular multilevel converter," *IEEE Trans. Power Electron.*, vol. 35, no. 4, pp. 3416–3433, Apr. 2020.
[22] D. Chen, Z. Feng, Q. Wang, L. Fang, and B. Bai, "Study of analysis and experiment for ability to withstand DC bias in power transformers," *IEEE Trans. Magn.*, vol. 54, no. 11, Nov. 2018, Art. no. 8401406.
[23] M. S. Diab, A. A. Elserougi, A. M. Massoud, S. Ahmed, and B. W. Williams, "A hybrid nine-arm modular multilevel converter for medium-voltage six-phase machine drives," *IEEE Trans. Ind. Electron.*, vol. 66, no. 9, pp. 6681–6691, Dec. 2019.
[24] W. Yang, Q. Song, S. Xu, H. Rao, and W. Liu, "An MMC topology based on unidirectional current H-Bridge submodule with active circulating current injection," *IEEE Trans. Power Electron.*, vol. 33, no. 5, pp. 3870–3883, May 2018.
[25] S. Du, B. Wu, and N. Zargari, "Common-Mode voltage minimization for grid-tied modular multilevel converter," *IEEE Trans. Ind. Electron.*, vol. 66, no. 10, pp. 7480–7487, Oct. 2019.
[26] M. Hagiwara and H. Akagi, "Control and experiment of pulse width modulated modular multilevel converters," *IEEE Trans. Power Electron.*, vol. 24, no. 7, pp. 1737–1746, Jul. 2009.

Futian Qin (Student Member, IEEE) received the B.Eng. degree in electrical engineering from Shandong Agricultural University, Tai'an, China, in 2015. He is currently working toward the Ph.D. degree in electrical engineering from Shandong University, Jinan, China.

From December 2019 to June 2020, he was a Research Assistant at Energy Research Institute @ Nanyang Technological University, Singapore. His research interests include modular multilevel converter (MMC), Nine-arm MMC, HVdc, and FACTS.

Feng Gao (Senior Member, IEEE) received the B.Eng. and M.Eng. degrees in electrical engineering from Shandong University, Jinan, China, in 2002 and 2005, respectively, and the Ph.D. degree from the School of Electrical and Electronic Engineering, Nanyang Technological University, Singapore, in 2009.

From 2008 to 2009, he was a Research Fellow at Nanyang Technological University. Since 2010, he has been with Shandong University, where he is currently a Professor with the School of Control Science and Engineering. From September 2006 to February 2007, he was a Visiting Scholar at the Department of Energy Technology, Aalborg University, Aalborg, Denmark.

Dr. Gao was the recipient of the IEEE Industry Applications Society Industrial Power Converter Committee Prize for a paper published in 2006 and 2017 IEEE Power Electronics Transactions Second Prize Paper Award. He is currently serving as the Associate Editors of IEEE TRANSACTIONS ON POWER ELECTRONICS and *CPSS Transcations on Power Electronics and Applications*.

Yi Tang (Senior Member, IEEE) received the B.Eng. degree in electrical engineering from Wuhan University, Wuhan, China, in 2007, and the M.Sc. and Ph.D. degrees from the School of Electrical and Electronic Engineering, Nanyang Technological University, Singapore, in 2008 and 2011, respectively.

From 2011 to 2013, he was a Senior Application Engineer with Infineon Technologies Asia Pacific, Singapore. From 2013 to 2015, he was a Postdoctoral Research Fellow with Aalborg University, Aalborg, Denmark. Since March 2015, he has been with Nanyang Technological University, Singapore, as an Assistant Professor. He is currently the Cluster Director of the Advanced Power Electronics Research Program at the Energy Research Institute, Nanyang Technological University.

Dr. Tang was a recipient of the Infineon Top Inventor Award in 2012, the Early Career Teaching Excellence Award in 2017, and four IEEE Prize Paper Awards. He currently serves as an Associate Editor for the IEEE TRANSACTIONS ON POWER ELECTRONICS (TPEL) and the IEEE JOURNAL OF EMERGING AND SELECTED TOPICS IN POWER ELECTRONICS (JESTPE).

Tao Xu (Member, IEEE) received the B.Eng. and Ph.D. degrees in electrical engineering from Shandong University, Jinan, China, in 2014 and 2019, respectively.

From 2017 to 2018, he was a Visiting Scholar at the Institute of Energy Technology, Aalborg University, Aalborg, Denmark. Since 2019, he joined the School of Electrical Engineering, Shandong University, where he is currently a Postdoc. His research interests include parallel inverters, power quality and modulation methods.

Dr. Xu was the recipient of the IEEE TRANSACTIONS ON POWER ELECTRONICS (PELS) Second Prize Paper Award in 2017 and the IEEE PELS Prize Ph.D. Thesis Talk in 2019.

Jinyu Wang (Member, IEEE) received the B.Eng. degree in electrical engineering and M.Eng. degree in power electronics from Jilin University, Changchun, China, in 2010 and 2013, respectively, and the Ph.D. degree in power system from Shandong University, Jinan, China, in 2017.

From July 2017 to June 2019, he was a Postdoctoral Research Fellow with Rolls-Royce Cooperate Lab@ Nanyang Technological University, Singapore, where he is currently a Research Fellow with the Energy Research Institute. His current research interests include power electronics, multilevel converters, renewable energy generation, and integration techniques as well as stability analysis and control of modular multilevel converter based HVdc.

Decun Niu (Student Member, IEEE) received the B.Eng. degree in electrical engineering from University of Jinan, Jinan, China, in 2011, and the M.Eng. degree in electrical engineering in 2014 from Shandong University, Jinan, China, where he is currently working toward the Ph.D. degree in electrical engineering.

From 2014 to 2018, he was an Electrical Designer in Shandong Engineering Consulting Institute Company Limited, Jinan, China. His research interests include multilevel converters, modulation methods, and FACTS.